ELSEVIER

Tectonophysics 333 (2001) 241–259

TECTONOPHYSICS

www.elsevier.com/locate/tecto

Paleoseismic event and active faulting: from ground penetrating radar and high-resolution seismic reflection profiles across the Chihshang Fault, eastern Taiwan

J. Chow[a,*], J. Angelier[b], J.-J. Hua[a], J.-C. Lee[c], R. Sun[d]

[a]*Institute of Applied Geophysics, National Taiwan Ocean University, Keelung, Taiwan, ROC*
[b]*Tectonique Quantitative, Département de Géotetonique and U.R.A, 1759, University P. and M. Curie, Boîte 129, 4 pl. Jussieu, 75252 Paris Cedex 05, France*
[c]*Institute of Earth Sciences, Academia Sinica, Taipei, Taiwan, ROC*
[d]*Department of Earth Sciences, National Chenkung University, Tainan, Taiwan, ROC*

Abstract

Ground penetrating radar (GPR) and high-resolution shallow seismic reflection have been carried out to delineate the subsurface pattern and paleoseismic facies of the active Chihshang Fault, a segment of the Longitudinal Valley Fault, eastern Taiwan. Optimum radar results were obtained along streets in the Chinyuan village. A total of 720 m GPR profiles were acquired with 200 MHz antenna. Two seismic sections were collected using Mini-Sosie sources, providing a frame to the radar profiles.

Three types of structures revealing evidence for a paleoseismic event can be observed in one GPR profile; these are: upward fault termination, colluvial wedge, and sand injection. Other profiles reveal unconformities, reverse-faults, one fault-related fold, and the presence of a colluvial wedge on the downthrown block, all indicating paleoseismic activity.

The remarkable feature of the Chihshang Fault at Chinyuan is that the dips of this active fault at surface changes rapidly along strike. Combining the GPR with shallow seismic reflection allows us to reconstruct the three-dimensional fault pattern of the Chihshang Fault and resolve doubts about the abrupt changes of fault dips. These GPR and seismic studies are consistent with the surface observation and reveal the complicated pattern of antithetic subsidiary faults in the near-surface part of the major E-dipping Chihshang thrust fault.

Keywords: active fault; ground penetrating radar; high-resolution shallow seismic; Taiwan

1. Introduction

The Chihshang Fault is situated in the central portion of the Longitudinal Valley of eastern Taiwan (Fig. 1), and is one of the most active segments in a fault system which occupies a suture zone between the Philippine Sea plate and Eurasia. The Longitudinal Valley, the present geomorphic expression of the suture, is a major NNE-trending linear feature approximately 160 km long which separates the high Central Range to the west and the Coastal Range to the east. Both mountain ranges are part of the Taiwan orogenic belt, formed by SE–NW convergence between the Philippine Sea plate and Eurasia. There are numerous field evidences of recent fault activity in the Longitudinal Valley (Hsu, 1962a), especially along the segment of the Chihshang Fault (Barrier

* Corresponding author. Fax: +886-2-24-62-50-38.
E-mail address: jdchow@ms24.hinet.net (J. Chow).

0040-1951/01/$ - see front matter
PII: S0040-1951(00)00277-8

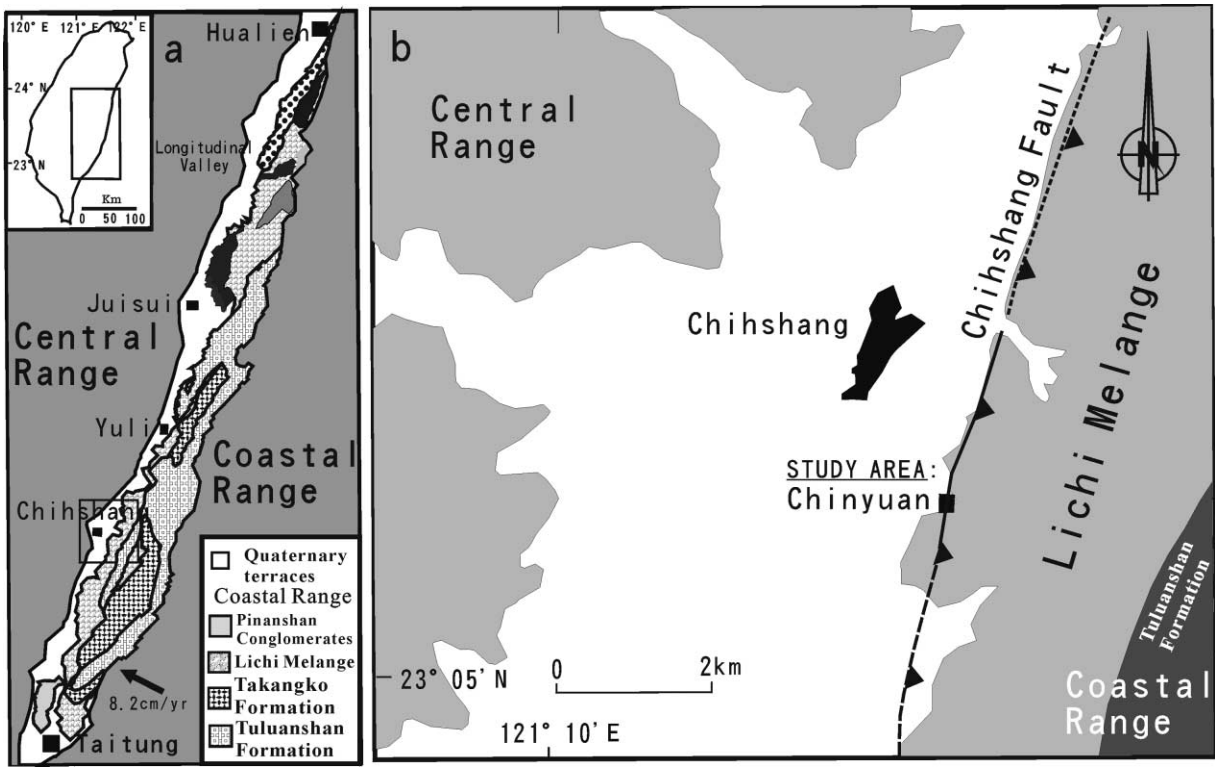

Fig. 1. General geological map of the Longitudinal Valley and the Chihshang Fault area (after Angelier et al., 1997). (a) General geological map of the Longitudinal Valley between the Central Range of Taiwan (to the west) and the Coastal Range (to the east). Insert figure on topleft showing the location. (b) Geological map of the Chihshang area. Main geological formations, from west to east: metamorphic basement of the Central Range, late Quaternary alluvium of the Longitudinal Valley, Pliocene Lichi Mélange (commonly overlain by Quaternary terraces) and Miocene Tuluanshan Formation. Active fault trace: thick line.

and Chu, 1984; Chu et al., 1994). Detailed qualitative and quantitative studies of active creep behaviors along the Chihshang Fault is well documented (Yu et al., 1990; Lee and Angelier, 1993; Angelier et al., 1997).

Because of excellent surface exposures near the Chinyuan Village, the Chihshang Fault in that area has received extensive study, including geodetic measurement (Yu and Liu, 1989; Yu et al., 1997), site investigation (Lee, 1994; Angelier et al., 1997), and an electrical resistivity study for road planning by Industrial Technology Research Institute (Chu and Yü, 1997). The aim of the present study was to obtain subsurface data from ground penetrating radar (GPR) and high-resolution seismic reflection which could provide supplement data to previous studies and permit a more detailed understanding of the structure and the evolution of the active Chihshang Fault (Fig. 2). The methods we adopted yield high-resolution data (0.2 m for GPR and 4 m for high-resolution seismic reflection) because the resolution of conventional seismic reflection methods (40 m) is insufficient to detect the relatively small displacements produced by paleoseismic events along the fault.

2. The active Chihshang Fault

The Chihshang Fault is a N018°E-trending reverse-fault with a left-lateral component of relative movement. The surface dip of the fault at one outcrop north of Chihshang, approximately 45° to the east, is consistent with the distribution of earthquake foci, which indicate a dip of approximately 55° in the crustal scale about 40 km deep (Tsai et al., 1977). The fault is associated with recent earthquake activity (e.g. the

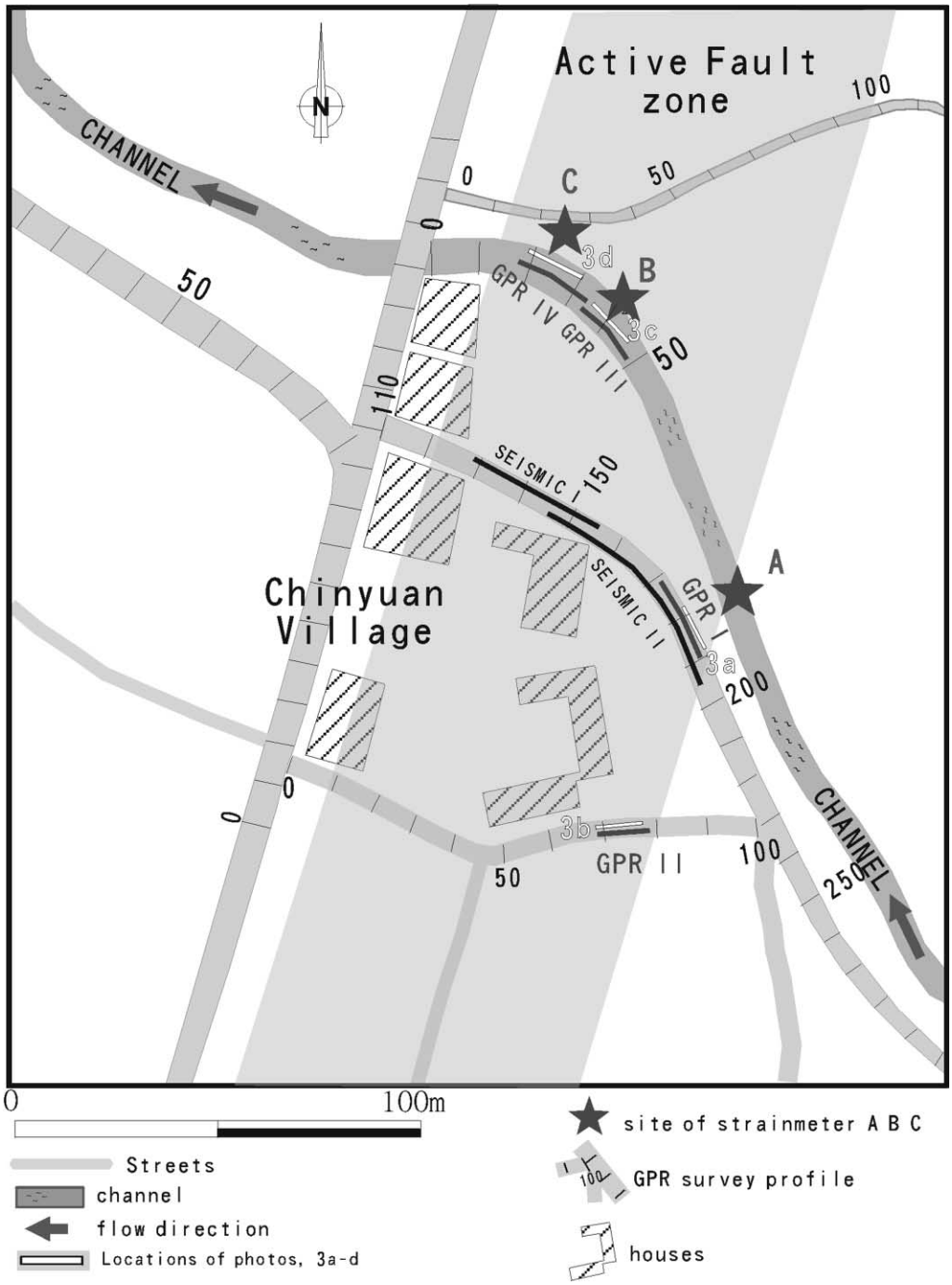

Fig. 2. Location map of the GPR survey and the high seismic reflection lines in Chinyuan village, including GPR I, GPR II, GPR III, GPR IV, SEISMIC I, and SEISMIC II. The survey lines are marked at every ten meters.

1951 $M = 6.8$ Taitung earthquake). Other evidence for recent activity along the fault includes a steep, straight scarp that is obviously non-erosional in origin (Hsu, 1962b). In some places, such as Chinyuan, the fault clearly affects Holocene valley deposits.

Where the fault can be mapped on the surface, it forms the western boundary of the Coastal Range, and separates Quaternary river terraces on the west, from the Pliocene Lichi Mélange on the east (Fig. 1); the latter consists of exotic blocks of varied lithologies (volcanic, ophiolitic, and sedimentary rocks) in a matrix of marine clay and mudstone (Chen, 1991) and has been interpreted as a product of subduction and collision (Chen, 1988, 1991; Huang et al., 1991). Along the fault, Lichi Mélange in the hanging wall overthrusts Quaternary alluvium of the Longitudinal Valley. The alluvium consists mainly of braid-bar deposits of gravel and sand which form the terraces of the Pinantahsi River, many of which are Holocene in age.

The surface geometry of the Chihshang Fault and its motions are known from field observations and geodetic analysis (Lee and Angelier, 1993; Angelier et al., 2001). The fault crops out clearly near Fuli as a single surface at the eastern edge of the Longitudinal Valley (Barrier and Chu, 1984; Angelier et al., 1997). Recent surveys along the Chihshang Fault, indicate a vertical displacement velocity of approximately 1.3 cm/yr, with an actual oblique offset of 2.6 cm/yr (Angelier et al., 2001). In the horizontal plane, slip velocity is rather constant, at 2.2 cm/yr in a N040°W direction, and involves both a thrust component with a horizontal shortening of nearly 1.7 cm/yr and a left-lateral component of nearly 1.4 cm/yr (Angelier et al., 2001).

In contrast to the single surface observed near Fuli, the Chihshang Fault in the vicinity of Chinyuan Village consists of a 50-m wide fault zone. In the village of Chinyuan, numerous faults and fractures affect walls, houses, and roads (Fig. 3). Three strainmeters installed across the three main fault branches demonstrate that creep is the dominant fault behavior at the present time (Lee et al., 2001). No large ($M > 6$) earthquakes have occurred in this area since 1951. Although geophysical corroboration is lacking, it is assumed that the 1951 Taitung earthquake ended a period in which compressive stress accumulated under the conditions of a locked fault and initiated the current period of creep (Angelier et al., 2001).

At Chinyuan, long-term site surveying allowed accurate reconstruction of the evolution of slip with time for more than 10 years (Lee, 1994; Angelier et al., 1997). The survey indicated a rather stable velocity of horizontal shortening, 1.9 cm/yr, resulting in a total displacement of about 21 cm in about 9.5 years (Angelier et al., 1997, 2001).

We thus use this site survey as a basis of our study of geophysical approaches. We aim at providing information on shallow subsurface structures of the Chihshang Fault by comparing the surface features in a more detailed way.

3. Methodology

3.1. Ground penetrating radar

The present GPR survey in the Chinyuan area consisted of a total of 720 m of survey lines laid out on road surfaces and on the beds of concrete stream channels in such a way as to cross the trace of the active faults, as determined from the detailed field studies of Angelier et al. (1997). Field work was carried out during the dry season to avoid damage by water flow in the stream channels. Data were collected using a SIR-2 digital GPR system manufactured by Geophysical Survey Systems, Inc. To optimize depth of penetration, we used 200 MHz antennae with continuous mode. Profiles were processed and plotted with GSSI RADAN software equipped with band-pass filter, gain control, distance normalization, and hyberbola migration. Technical aspects of the GPR method have been described in detail in Appendix A.

3.2. High-resolution seismic reflection

Because GPR is capable of penetrating only to depths of 5 m, we supplemented the GPR survey with two, high-resolution (4 m resolution) seismic reflection lines to obtain data from greater depths. This type of seismic reflection is capable of penetrating to depths of 60–300 m. We utilized two high-resolution seismic reflection lines in the Chihshang area. Data were acquired by using Mini-Sosie sources and a Geometrics Strata View 48 channel

seismograph recorder. The seismic profiles were obtained by a standard data processing procedure. Detailed description of high-resolution seismic reflection can be seen in Appendix B.

4. Results

4.1. GPR profiles

Four GPR profiles (GPR I, GPR II, GPR III, and GPR IV) have been selected to illustrate the structure of the Chihshang Fault; in the other profiles, the faults were either hard to locate or the data was of poor quality because of electrical interference from nearby power lines. The penetration depth on these profiles is approximately 4.5 m, according to an estimate based on the dielectric constants. In each of the profiles, the various reflectors were identified, and the inferred stratigraphic layers were numbered and analyzed for lateral continuity. For example, in GPR I, some of the units (e.g. Unit 3) are continuous; others (e.g. Units 11b and 11c) are lenticular, some pinch out (e.g. Unit 21), and others are disrupted by faulting (e.g. Unit 15).

4.1.1. Profile GPR I

Survey line GPR I passes close to strainmeter A, where the fault branch crosses the wall of the stream channel. Profile GPR I clearly shows a W-dipping reverse-fault reaching almost to the ground surface near distance marker 188 m (Fig. 4). This fault does in fact have surface expression, observable in the fracturing in the channel wall (Fig. 3a). On GPR I, the fault dip is seen to be changed markedly below the depth of the Unit 13 reflector.

On profile GPR I, paleoseismic events can be inferred by three types of evidence: the upward termination of faults, colluvial wedges, and sand injection (the latter defined by Allen, 1986). For instance, at distance marker 178 m, a southeast-dipping normal-fault terminates at Unit 15, 3 m below the surface. This termination suggests that a paleoseismic event occurred, following the deposition of Unit 15: the event formed a fault scarp, and erosion of the upthrown block was the source for a colluvial wedge, represented by Units 13 and 14, which was deposited on the downthrown block and eventually buried the fault. Units (11a, 11b, 11c, 11d, 11e) overlying the colluvium experienced slight folding at a later time, possibly during the injection of a sand sill during a later, stronger seismic event associated with the above-mentioned major reverse-fault. These mildly fold-deformed units are both underlain and overlain by undeformed, nearly horizontal strata.

4.1.2. Profile GPR II

Profile GPR II is located on the pavement of a road near a farmhouse in Chinyuan village (Fig. 2). In contrast to GPR I, however, the profile shows an E-dipping reverse-fault (Fig. 5). Most of the reflectors observed on the profile are nearly planar and parallel. Although the fault displacements are not large, the discontinuity of the reflector units along the fault is obvious. The reverse character of the main fault can still be determined by the offsets of multiple stratigraphic units. Although most of the reflecting horizons are planar, some deformation can be observed in Units 11–13, particularly within the hanging wall block of the reverse-fault. The soft sediments in the footwall adjacent to the fault surface have also been deformed by drag along the fault. Deformation of Units 11–13 is in fact observed in all four GPR profiles and it seems likely that these units were affected by penecontemporaneous deformation during their deposition.

4.1.3. Profile GPR III

Profile GPR III follows the bed of the stream channel where it crosses a fault trace. Between distance markers 36 and 48 m, near the location of strainmeter B (Fig. 2), the profile reveals a fold-and-thrust geometry in Units 11–13 (Fig. 6). The fold is asymmetrical, with a gentle back limb and a steep forelimb which dips to the NW; it appears to be a fault-related anticline. The underlying reverse-fault, branches into a complex system of synthetic and antithetic faults as it extends upward. The subsurface structure is mimicked at the surface by similar features on the wall of the stream channel at the location of strainmeter B (Fig. 3c).

4.1.4. Profile GPR IV

Profile GPR IV (Fig. 7) is located just west of GPR III (Fig. 2). Where the profile crosses the other fault trace, there is disruption of all the strata. As in GPR III, there is a small-amplitude fault-bend fold in Units

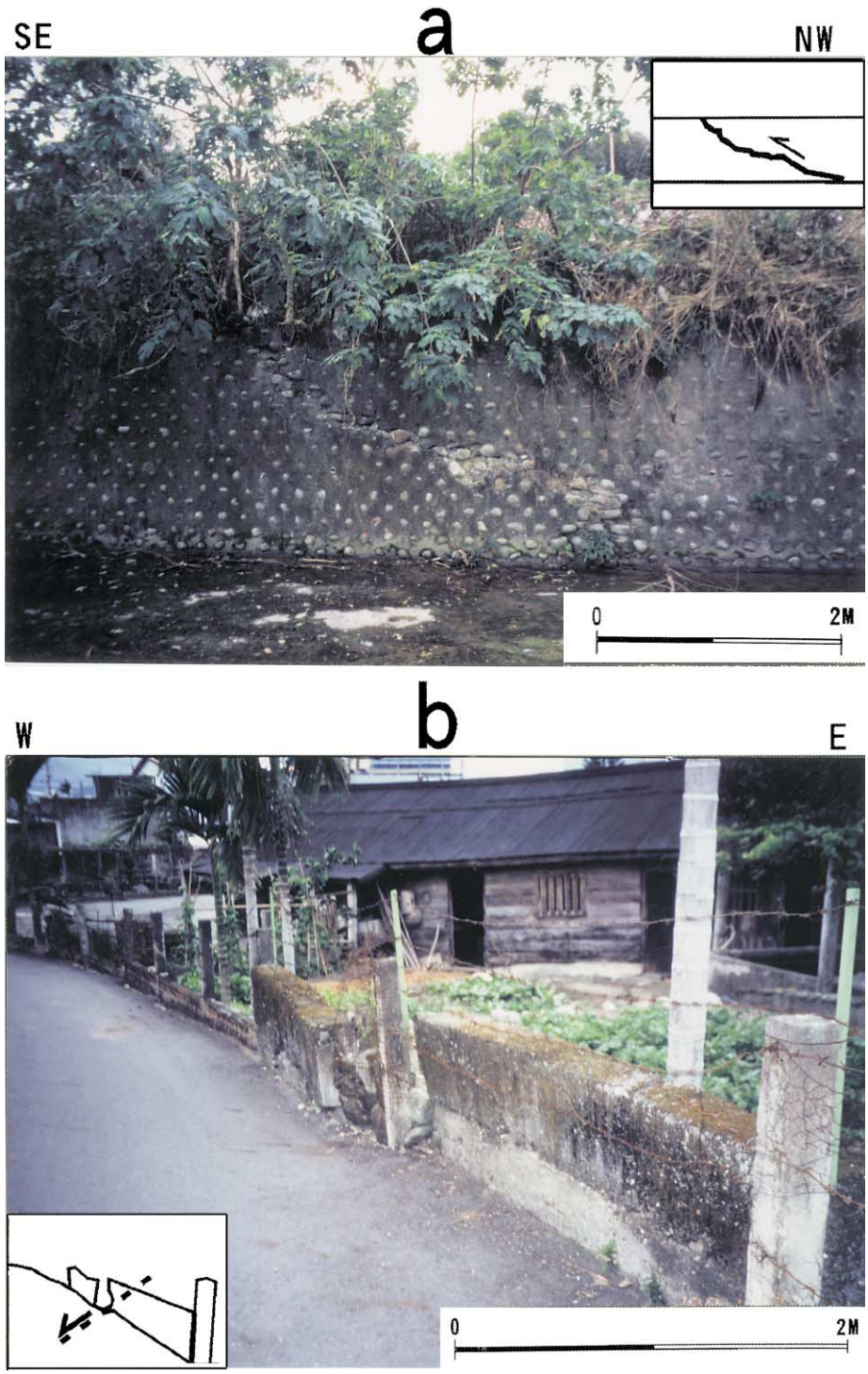

Fig. 3. Photographs of the active fault branches and fractures of Chihshang Fault at the surface, corresponding to structures in the GPR and seismic profiles. Location see Fig. 2. (a) W-dipping active fault in the channel wall opposite to strainmeter A. Right and left of the photo need to be reversed in imagination, for easy comparison with the profile GPR I (Fig. 4). (b) Strike–slip component (left-lateral) of the active fault recorded by the offset of a wall and its fence along a street. The location of this photo is that of GPR II in Fig. 2.

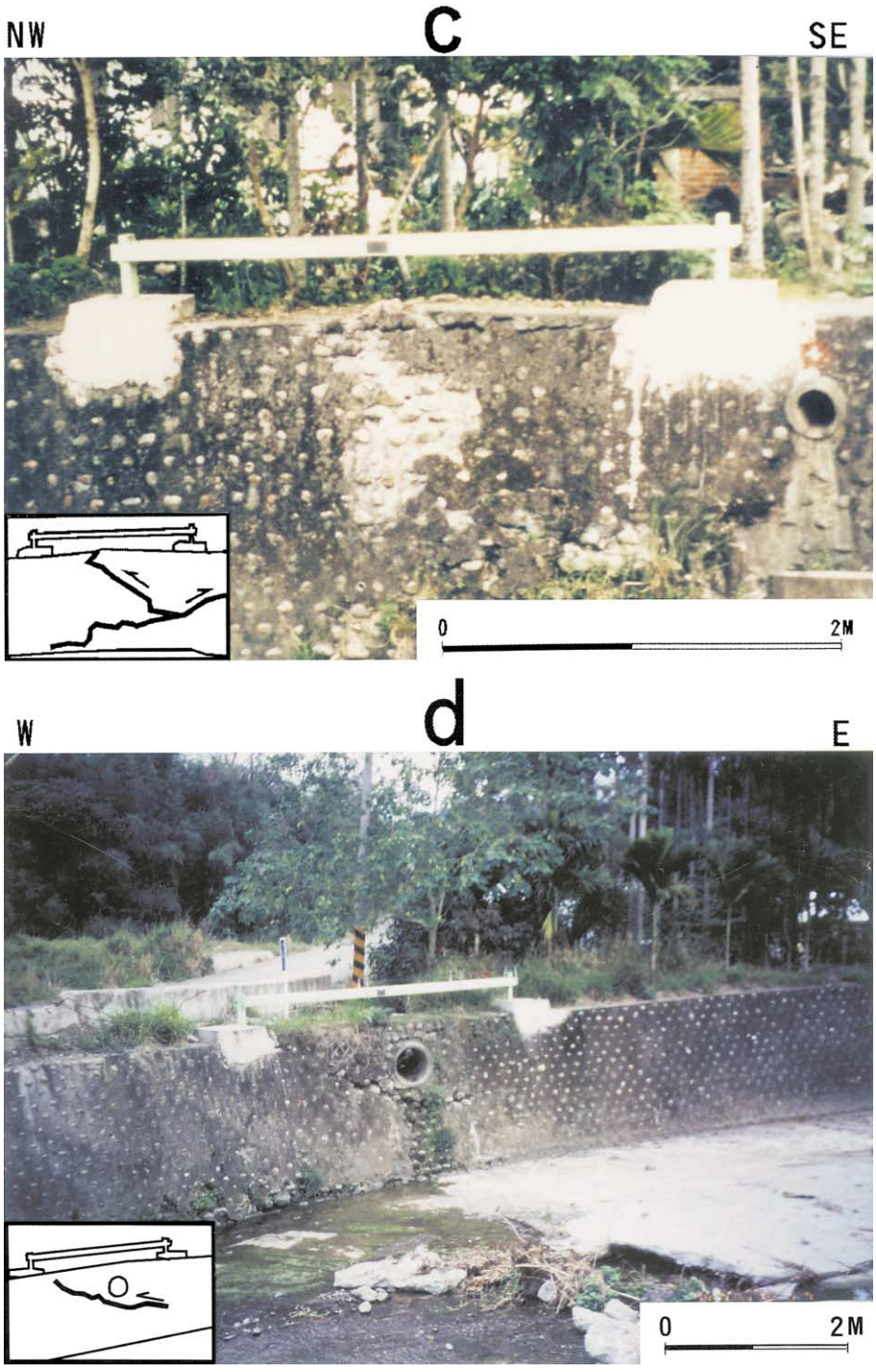

Fig. 3. (c) E-dipping reverse-fault fractures in the channel wall below strainmeter B (visible in picture). Location is the same as for GPR III survey line. (d) E-dipping fault fracture in the channel wall below strainmeter C. Location as for the GPR IV survey line.

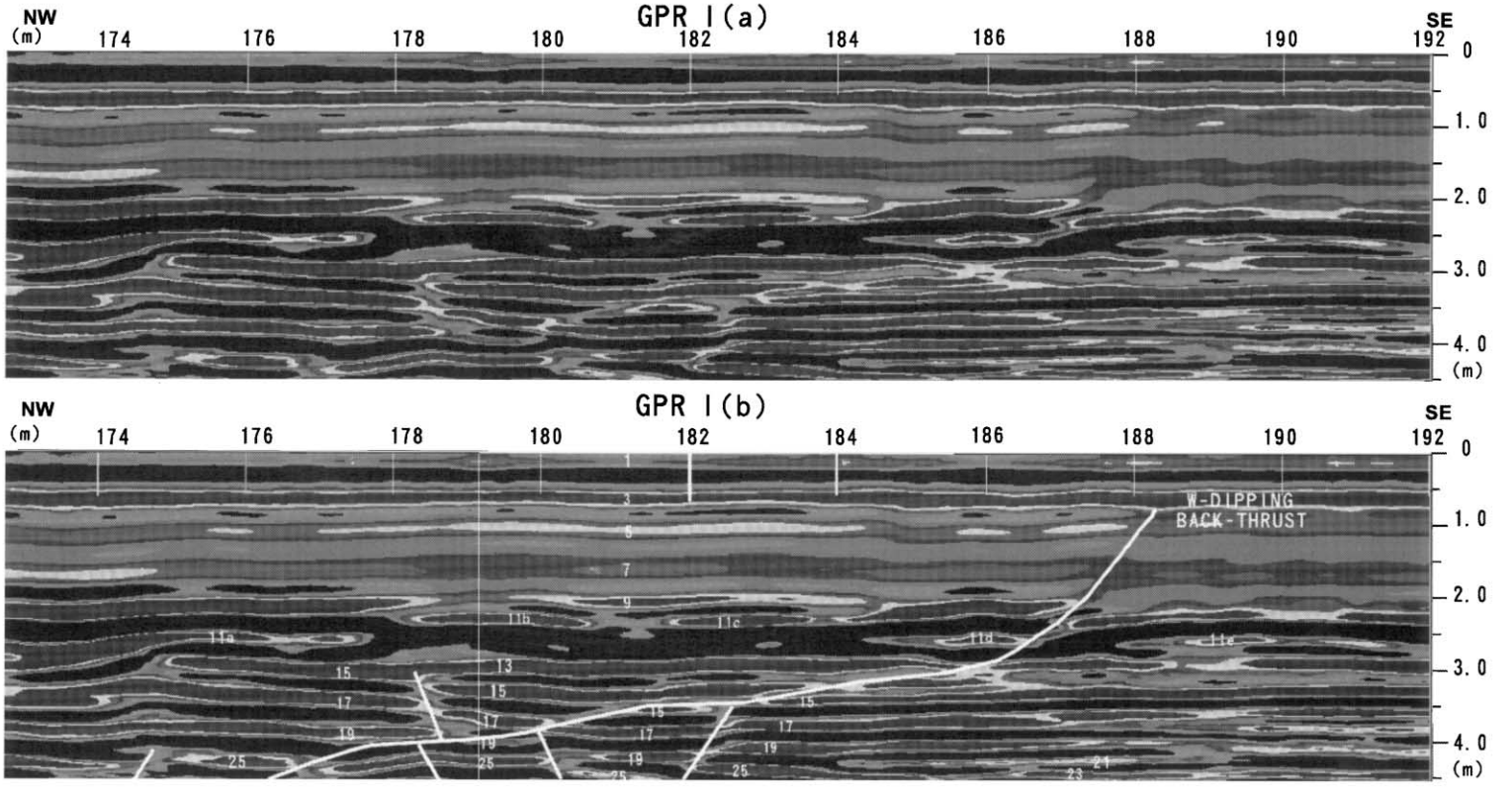

Fig. 4. GPR profile I: (a) uninterpreted profile; (b) interpreted profile showing the NW-dipping back thrust fault (emerging at the place where the picture of Fig. 3a was taken). Note also the presence of few minor normal-faults. Three types of stratigraphic indicators (upward fault termination, colluvial wedge and sand injection) yield evidence for a paleoseismic event. Numbers in white refer to identified layer units. Note that Units 1 and 2 in Figs. 4 and 5 are the GPR direct wave, not stratigraphic signals. The marks on the top of the profile in metres correspond to the metric marks in the map of Fig. 2. The depth scale, in metres, is shown on the right.

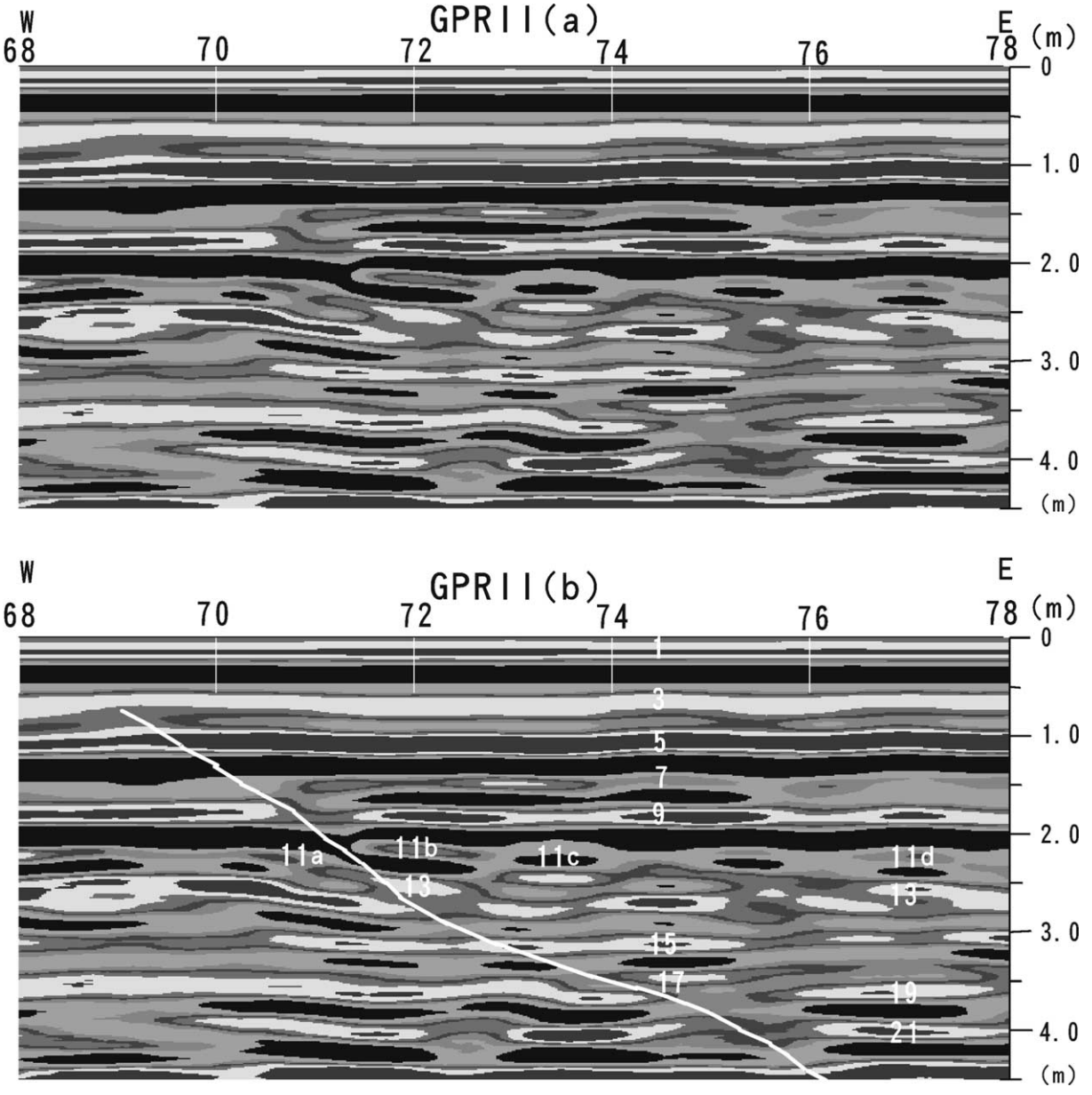

Fig. 5. GPR profile II: (a) uninterpreted profile; (b) interpreted profile showing the E-dipping reverse-fault that break the surface at the place where wall and fence are offset in Fig. 3b. Other explanations as for Fig. 4.

11–13 in the hanging wall of the fault, this appears to reflect minor folding during fault activity. Slumping and flow of eroded material from the upthrown blocks created a wedge of colluvium in the downthrown block. Unit 13 in the upthrown block corresponds to an expanded section in the downthrown block which includes Units 13 and 13a. These observations indicate the existence of a colluvial wedge, one of the evidences of paleoseismic activity.

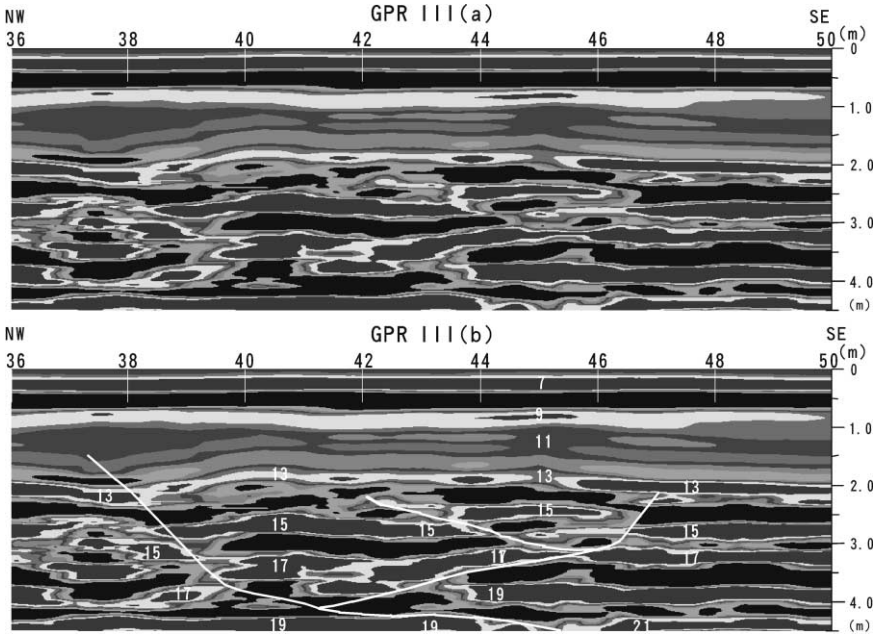

Fig. 6. GPR profile III: (a) uninterpreted profile; (b) interpreted profile showing synthetic and antithetic faults that merge at shallow depth (4 m). The upwarping of the small pop-up structure thus defined. This structure corresponds to the surface deformation shown in Fig. 3c. Note that the shape of the deformed layers resembles the ground deformation pattern at the same location. The GPR direct wave corresponds to Units 7 and 8 in this profile, which was surveyed on the dry beds of concrete stream channels not on the banks. Other explanation as for Fig. 4.

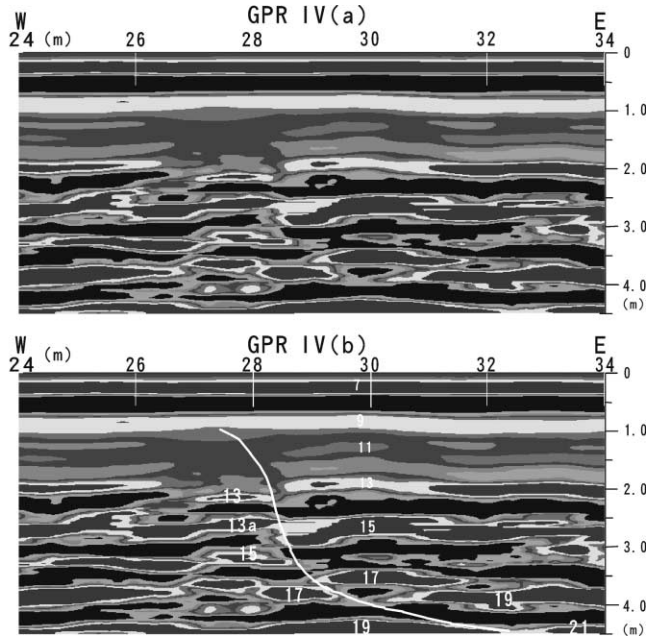

Fig. 7. GPR profile IV: (a) uninterpreted profile; (b) interpreted profile showing a E-dipping reverse-fault. Compare with the fracture in the channel wall in Fig. 3d. Other explanations as for Fig. 4.

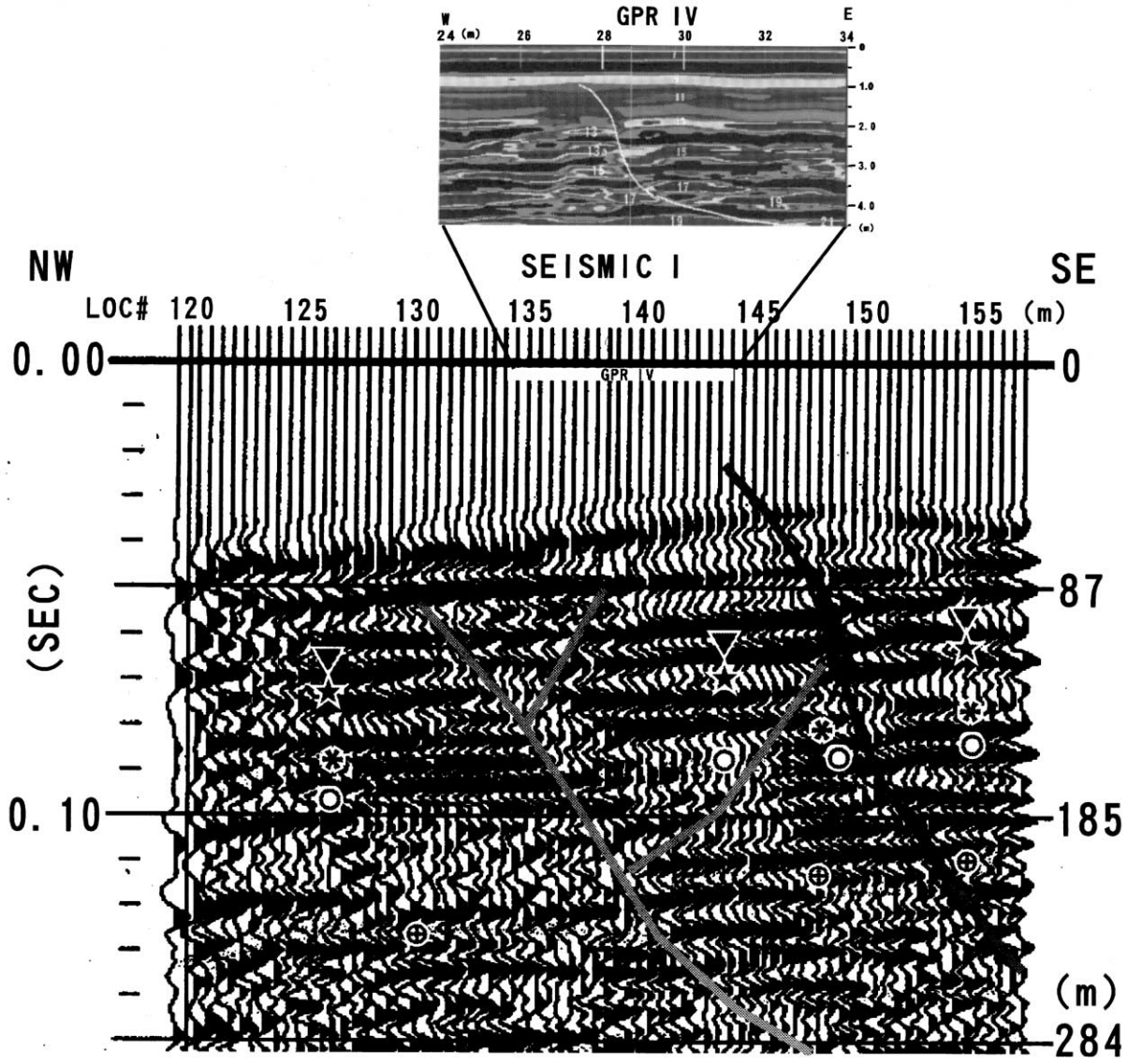

Fig. 8. Seismic section I showing SE-dipping reverse-faults associated with small antithetic reverse-faults. The symbols indicate correlated strata on the two sides of the reverse-fault. The blanked-out band at the top of the section shows the vertical and lateral extents of the GPR profile IV (shown above; see Fig. 7 for more details). Locations of seismic section I and GPR profile shown in Fig. 2.

4.2. Seismic reflection profiles

Seismic sections I (SEISMIC I) and II (SEISMIC II) are located along a street in Chinyuan (Fig. 2). As SEISMIC I (Fig. 8) shows, the strata, as observed from the surface to a depth of 0.15 s, dip gently to the west and are offset by several faults. In addition to two main SE-dipping reverse-faults, two NW-dipping antithetic faults can be observed on the profile. An E-dipping reverse-fault is also visible in SEISMIC II (Fig. 9); in this section, stratigraphic signals have been identified with symbols on both sides of the fault in order to give the sense of displacement. A comparison of the two blocks indicates reverse

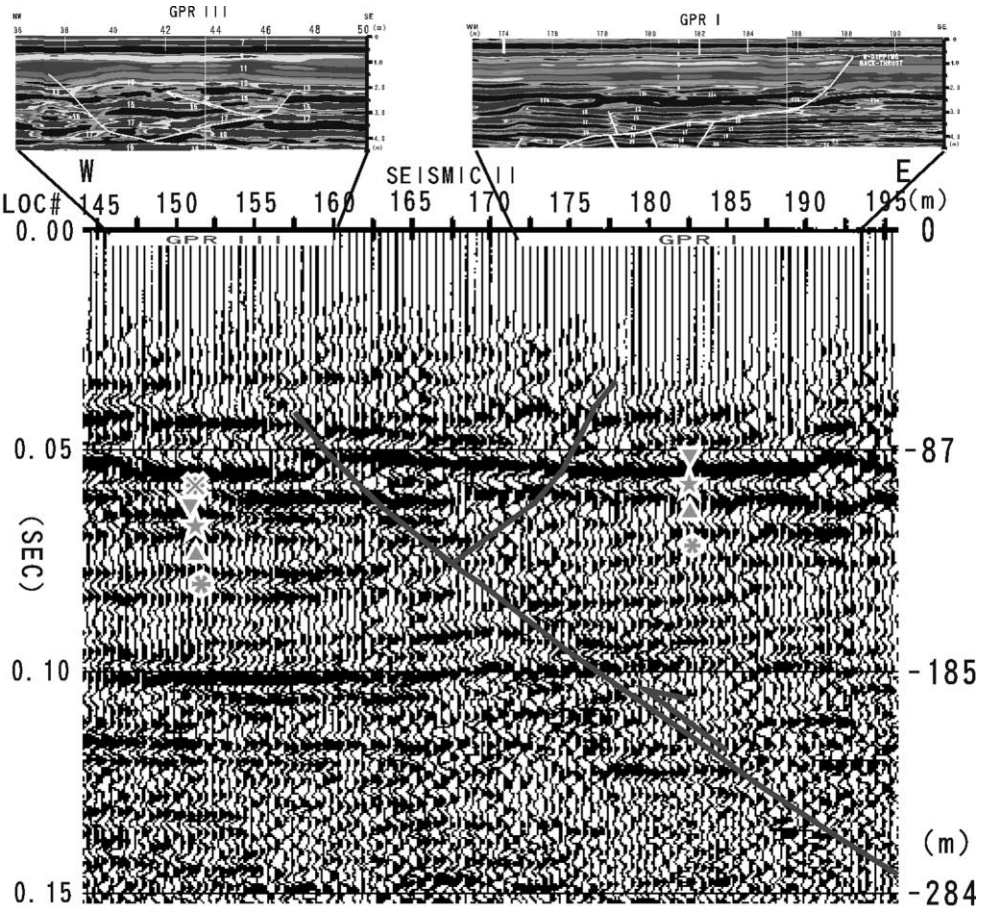

Fig. 9. Seismic section II showing a E-dipping reverse-fault with a smaller antithetic fault. The symbols indicate correlated strata on both sides of the fault. Blanked-out bands near top of the section show vertical and lateral extents of GPR profiles I and III (shown above; see Figs. 4 and 6, respectively, for more detail).

movement. Stratigraphic signals above the '※' unit are disturbed by refraction, and are largely missing. The amplitudes of the '▼' stratigraphic signals are stronger on the upthrown side of the fault, because the unit lies at shallower levels on this side and thus produces stronger seismic reflection. Faulting at depths less than 0.05 s (i.e. less than 100 m in depth) does not involve displacements large enough to be clearly detected in the seismic sections. Thus, these faults can only be delineated by the termination of reflectors or by changes in the dip of stratigraphic layers.

4.3. Comparison of GPR and seismic reflection results

Profile GPR I is parallel to section SEISMIC II and is separated from it by only a few meters (Fig. 2). Profiles GPR III and GPR IV are only 75 m from section SEICMIC I and can be correlated with that section. The location and depth of penetration of the GPR profiles relative to the seismic sections are shown by the blanked-out bands in Figs. 8 and 9.

Viewed together, section SEISMIC II and the overlying GPR profiles in Fig. 9 depict a single E-dipping reverse-fault which develops upward into a more complicated system of antithetic-synthetic faults and associated minor folding near the surface, as represented in Profile GPR III (Fig. 6). Minor folding is observed in the near-surface portions of the hanging wall side of the reverse-fault, both in GPR III (Units

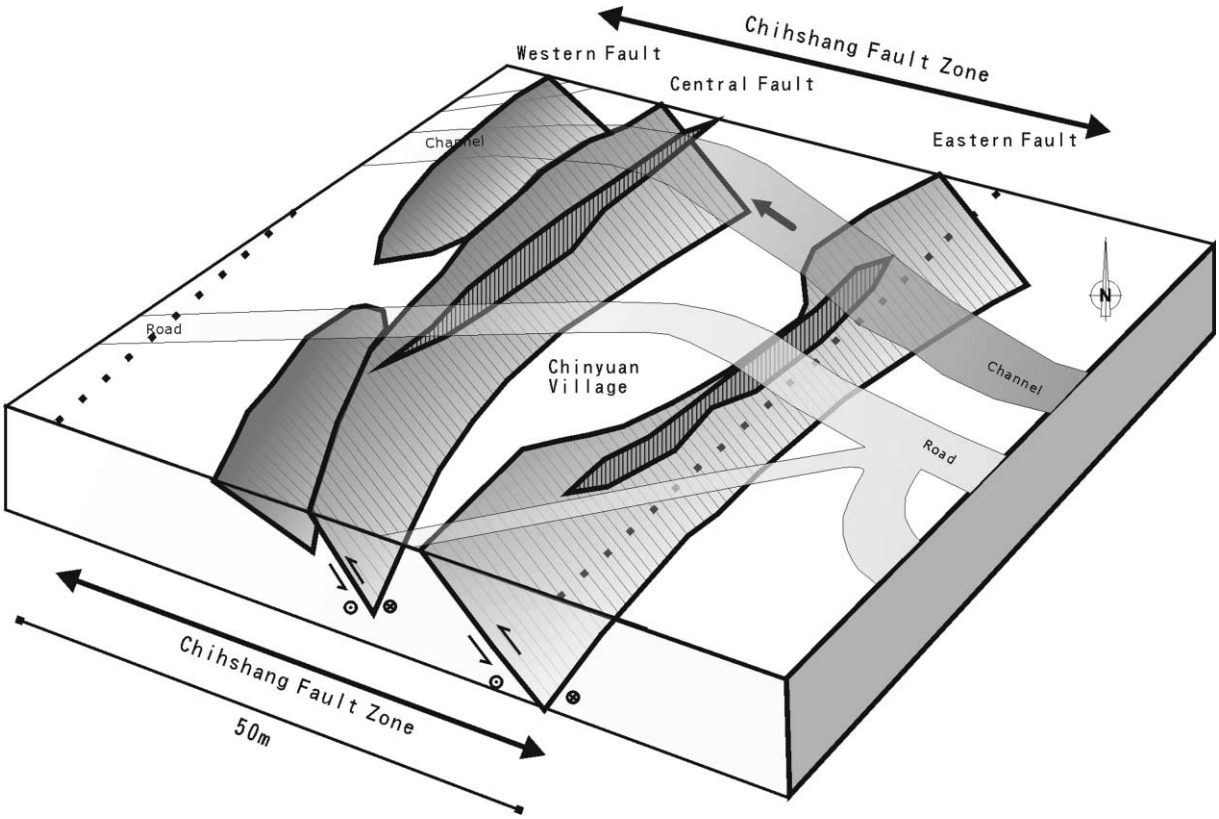

Fig. 10. Schematic 3D view of the fault distribution at Chinyuan. Compare with the map of Fig. 2 and the profiles of Figs. 4–9. Note that although the main faults dip to the east (with minor component of left-lateral motion), the dip direction of the faults may change abruptly near the surface, thus defining small pop-up structures. Note also that the dip of the reverse-fault at the surface may change rapidly along strike, such as in the middle sequence of the eastern fault.

11–13) and in surface exposures on the wall of the stream channel (Fig. 3c).

Comparison of the seismic sections and the GPR profiles (Figs. 8 and 9) highlights the complementary capabilities of the two techniques in identifying subsurface structural features. High-resolution seismic profiling has a deeper penetration capability than GPR, but loses detail in the shallower portions of the sections, where GPR is more effective in delineating minor structures.

5. Discussion

The results of the present study, when used in conjunction with those of previous studies of Angelier et al. (1997, 2001) permit a tentative three-dimensional (3D) reconstruction of the near-surface structure of Chihshang Fault Zone in the Chinyuan area (Fig. 10). The three major faults identified in previous studies (the Western Fault, the Central Fault, and the Eastern Fault) have all been delineated in the subsurface by the current study. The most remarkable feature identified in the course of this study is the presence of abrupt reversals of dip direction in the near-surface portions of the faults.

Such reversals have been previously suspected on the basis of field observations. Exposures of the Eastern fault in exposures in the walls of the Chinyuan stream channel indicate a startling change in dip direction from one side of the channel to the other: an E-dipping thrust appears on the north wall and a W-dipping thrust appears on the south wall, a change that occurs over a distance of less than 10 m. However, the

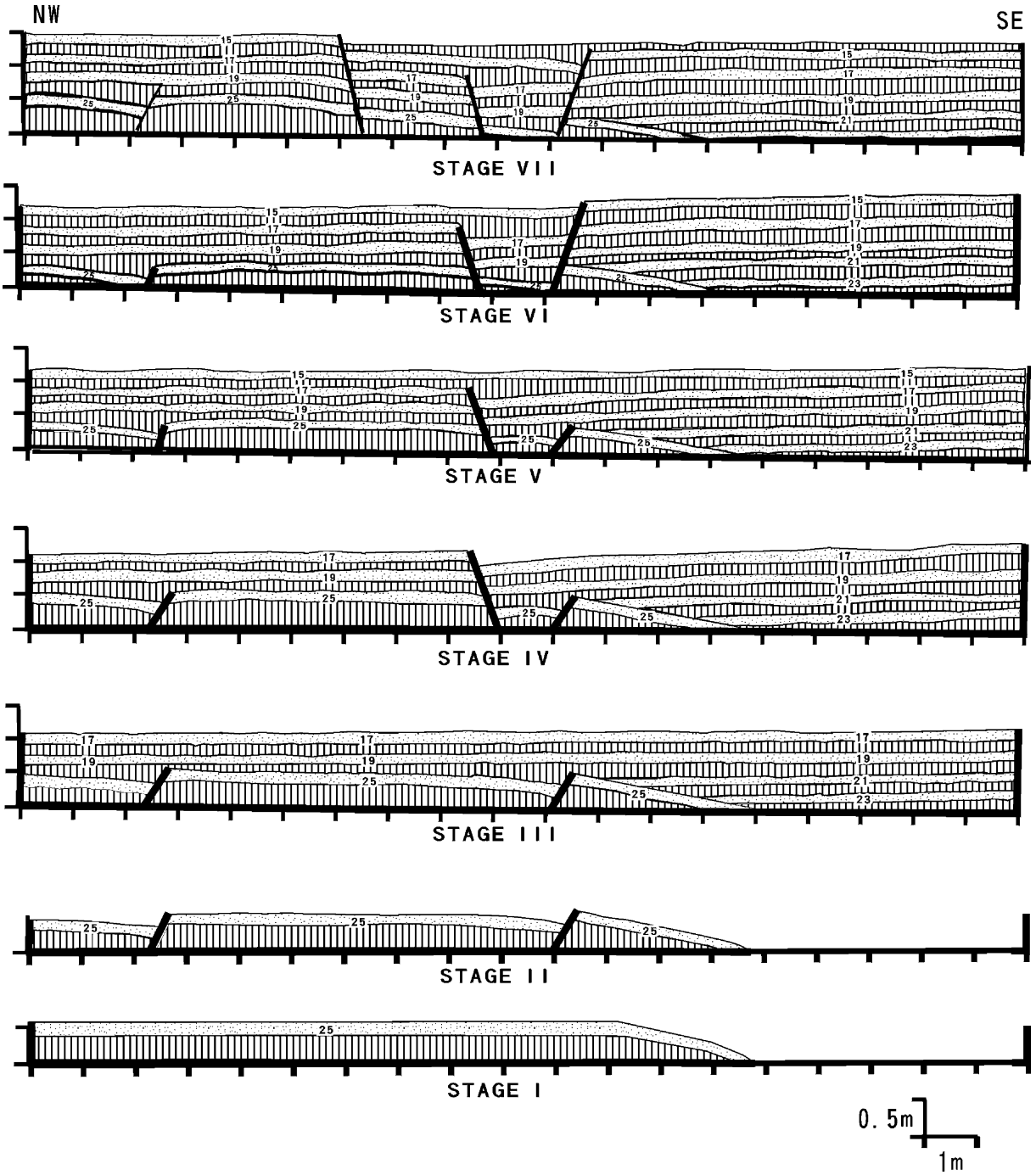

Fig. 11. Attempt at reconstructing in detail the evolution of faulting in the GPR I site (location in Fig. 2, GPR profile in Fig. 4) The reconstruction is based on layer identification in the radar profile. The stages were reconstructed by retrodeforming the sedimentary beds step by step, from XIII to I. The spacings between ticks represent 1 m for horizontal scale and 0.5 m for vertical scale. Each event horizon bed represents the ground surface at each step.

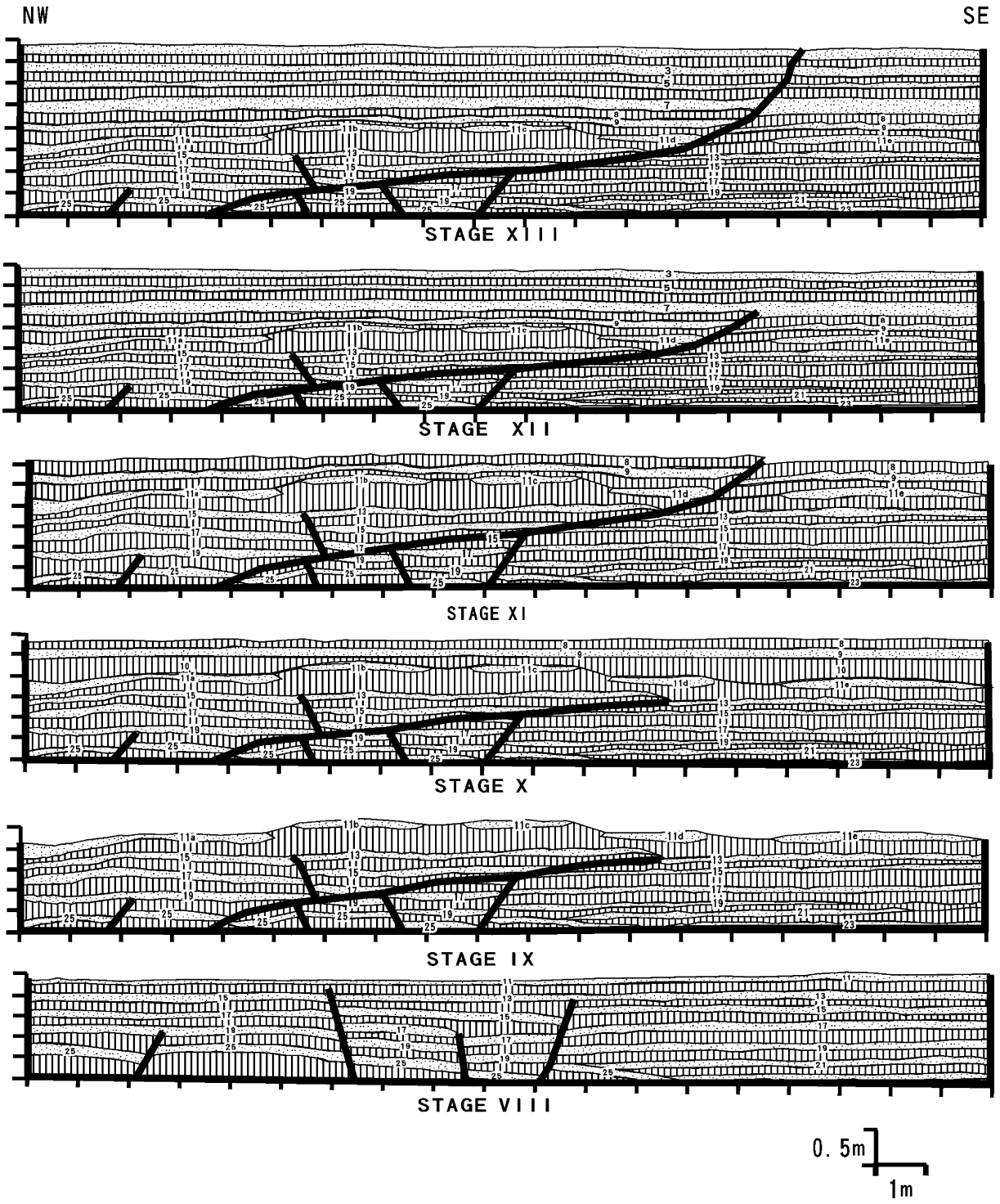

Fig. 11. (*continued*)

reliability of these surface observations can be called into question for two reasons. First, the faults are observed on near-vertical open surfaces which, by their nature, are subject to lateral changes in stress and strain. Secondly, they are observed in concrete walls and not in sediments, and may reflect structural effects within the walls which do not occur in the sediments. However, the GPR profiles support the validity of the surface observations. GPR I and GPR II cross the eastern fault, separated by a distance of only 50 m, but reveal different dip directions for the fault: E-dipping in GPR I and W-dipping in GPR II. From our profiles, the geometrical relationships between these near-surface breaks in the fault surface can be reconstructed; they are seen to form a pop-up structure approximately 20 m wide (Fig. 10). The profiles illustrate the complex structure of the uppermost portion of the faults, a complexity which is common along active faults with an oblique component of motion (reverse and left-lateral).

Profile GPR III (Fig. 6), which crosses the Central Fault, illustrates the complex interplay of antithetic and synthetic structures near the surface of the fault. The profile depicts two major reverse-faults, one E-dipping and the other W-dipping. The antithetic W-dipping fault merges into the E-dipping one at depth. At a shallower depth in the profile, a smaller synthetic E-dipping reverse-fault is visible and is seen to merge at depth with the larger, W-dipping reverse-fault.

When the structure of stratigraphic units between antithetic faults is examined in detail, flexure or warping (Allen, 1982) of the units is clearly visible. In profile GPR I, a low-amplitude fold is clearly expressed by the flexure of Units 11a, 11b, 11c, 11d, and 11e between 172 and 190 m (Fig. 4). The fold is symmetrical and has a wavelength of 13 m (from 174 to 187 m). According to a study by Audemard and de Santis (1991) of liquefaction structures produced by recent earthquakes, warping may to occur in the uppermost 0.2 m of sediment, where mud overlies thin sand beds. A similar report has been made by Sim (1973), who attributed the presence of low-amplitude folds in the uppermost 4–5 cm of lake sediment (mud with very fine sandy laminae and partings) to a magnitude 6.5 earthquake. Worldwide data from historical earthquakes indicate that liquefaction effects may accompany earthquakes with magnitudes as low as 5, but that such effects do not become widespread until magnitudes of 5.5–6 are reached (Ambraseys, 1988). Based on these observations, we infer that the low-amplitude folds observed in profile GPR I may be due to a magnitude 5 paleoearthquake. The fold could also have been produced by a quake-induced injection of liquefied sand. This origin is suggested in the case of the fold in GPR I, which is caused by a thickening of the layer intervening between Unit 11b/11c and Unit 13 (Fig.4). Prolonged or cyclic shearing of sediments during an earthquake can cause the pore fluid pressure in the sediments to exceed the static confining pressure, resulting in sudden liquefaction of the sediment–water mixture. Liquefaction is most likely to occur where sediments are water-saturated.

The geologic setting of the Chinyuan area makes it a likely site for quake-induced liquefaction. The geology of the uppermost 5 m of earth materials in the Chinyuan area is known from a 5-m deep trench which was excavated by Chu and Yü (1997). The trench exposed, from top to bottom, a thick topsoil, tens of centimeters thick, overlying a clay-rich chaotic mixture derived from the Lichi melange, which lay in turn above fluvial terrace deposits of presumed Holocene age. The present water table in the area is shallow ($<$3 m) and, based on past water levels in nearby Tapo Lake, the water table appears to have been shallow over a large area for most of the time period following deposit of the alluvial materials. Thus, in the Chinyuan area, the combination of a relatively shallow water table and widespread sand-rich fluvial deposits capped by fine-grained material derived from the Lichi melange increases the probability of liquefaction of near-surface materials during an earthquake.

Although seismic events and concomitant liquefaction may have played some role in producing the flexure and warping observed on the profiles, some structures could also been produced by permanent deformation accompanying creep (Angelier et al., 1997–1999). In particular, the gentle anticlines which are observed between conjugate reverse-faults that bound small pop-up structures may reflect this type of deformation.

One important aspect of the present study lies in its potential to reconstruct a detailed seismic history of the area, and thus to assist in the location

of future trenches across the active faults. From GPR I, the structural evolution of the Chinyuan area has been divided into thirteen stages (Fig. 11), as follows.

Stage I. Units 26 and 25 were deposited on an E-dipping surface (probably a tilted highland). Stage II. Several W-dipping normal faults formed, separating the sedimentary materials in Units 26 and 25 into tilted fault blocks. Stage III. Units 24–20 were deposited, as a sedimentary sequence onlapped the faulted surface from the east. Later, Units 19–17 covered the entire area conformably. Stage IV–V. Contemporary with the deposition of lower Unit 16, an E-dipping normal-fault offset the entire sedimentary sequence of that time (Units 26–17). Following the cessation of activity along this fault, the entire area was covered by upper Unit 16 and Unit 15. Stage VI–VII. Contemporaneous with the deposition of lower Unit 14, one of the W-dipping normal-faults active in Stage II was reactivated. At roughly the same time, the E-dipping normal-fault formed in Stage IV was also reactivated, and a fault scarp was formed. A colluvial wedge, represented by Units 13 and 12, was deposited on the downthrown side of the fault. Stage VIII. Unit 11 was deposited over the entire area. Stage IX. A low-angle, E-dipping reverse-fault propagated upward through Units 13–25. This vigorous seismic event triggered a sand injection, which in turn induced minor flexure of the overlying units. This sand injection was possibly emplaced via the reverse-fault itself, or from another fault in the vicinity. Stage X–XI. From the varying thickness of Unit 10 along the profile, it is inferred that the paleoseismic event responsible for Stage IX was immediately followed by the deposition of Unit 10 over the newly deformed ground surface. Following the deposition of Units 9 and 8, the reverse-fault reactivated and extended to the surface at a higher dip angle. The dip of the faulting is estimated to have been 30° in Stage X, steepening to 40° in Stage XI. Stage XII. Activity along the reverse-fault ceased, and Units 7–2 were laid down conformably over the entire area. Unit 1 is the direct GPR wave and does not represent a stratigraphic signal. Stage XIII. Due to intermittent reactivation, the reverse-fault propagated to the present-day surface.

In summary, profile GPR I shows major reverse-fault activity which climaxed in Stage X with sand injection. However, this reverse-fault activity was imposed on a background of minor normal-fault activity that was sufficient to produce some colluvial wedges.

6. Conclusions

The combination of GPR and high-resolution seismic reflection in our study of the Chihshang Fault Zone in the Chinyuan area demonstrates the complementary nature of these methods and their effectiveness in delineating subsurface structures and allowing 3D reconstruction of a complex structural zone. Such a study can also track the structural evolution of an area. Paleoseismic events can be inferred from profiles by three indicators: the upward termination of faults, colluvial wedges which collect on the downthrown side of fault scarps, and the presence of sedimentary injection sills.

Reverse-faulting dominated the neotectonics of the GPR I site, but was imposed on a background of minor normal-faulting which may possibly reflect the influence of nearby fault activity with a strike–slip component of movement. The three faults observed on the surface within Chihshang Fault Zone by previous workers were all identified in the subsurface by the current study, and were seen to have a constant eastward dip at depth. However, reverse-faults which appear as single E-dipping surfaces at depth appear to develop into complex structures near the surface. This apparent upward change may in part be resulting from the GPR resolution. However, increasing structural complexity upward no doubt to some degree also reflects a real change caused by a corresponding decrease in confining pressure as the free surface is approached.

Acknowledgements

Part of this work was carried out within the framework of a French–Taiwanese cooperative effort in the Earth Sciences, and was jointly sponsored by the French Institute in Taipei (FIT) and the National Science Council of Taiwan (NSC grant NSC 89-2116-M-019-001), including National Taiwan Ocean University, the Institute of Earth Sciences, Academica

Sinica, the University Pierre-et-Marie Curie (Paris) and the Central Geological Survey of Taiwan. We deeply appreciated J.C. Audru and H.T. Chu for their very constructive and thoughtful reviews.

Appendix A. Technique of ground penetrating radar

In the mid-1980s, researchers began to use analogue GPR to study faults (Bilham, 1985; Bilham and Seeber, 1985). Smith and Jol (1995) used digital GPR to study the Wasatch fault on the Elder Creek, Brigham. Profiling with GPR is similar to using sonar and seismic reflection methods, but the former is based on electromagnetic (EM) energy reflection (see Annan and Davis, 1976; Ulriksen, 1982; Daniels et al., 1988; Davis and Annan, 1989 for reviews). A short pulse of high frequency EM energy (usually in the 10–1000 MHz range) is transmitted into the ground, generating a wave front that propagates downward. Due to the change in the bulk electrical properties of different subsurface lithologies, mineralogy, and/or the character of the interface between different lithologies, some of the EM waves are reflected back to the surface (Davis and Annan, 1989; Moorman, 1990). At the surface a receiver monitors reflected energy versus delay-time. The pulse delay-time between the energy transmission into the ground and the reflection back to the surface is a function of the EM propagation velocity through the sediment and the depth of subsurface reflectors. GPR provides a profile of horizontal survey distance (m) versus vertical two-way travel time in nanosecond. The EM propagation velocity is determined by dielectric constants of sediments.

Contrasts in the dielectric constants of different sediment types usually cause reflections from lithologic boundaries in the subsurface. The magnitude of the reflected signal is basically proportional to the difference in dielectric constants of the sediment interface (Davis and Annan, 1989). Change in the dielectric constant also affects the rate of attenuation of energy passing through the ground. These effects enable the subsurface stratigraphy to be inferred from the character of the returning EM or radar signals.

Appendix B. Technique of high-resolution seismic reflection

The high-resolution seismic reflection data were collected using two Mini-Sosie sources. The Mini-Sosie consists of a hand-operated Earth tamper. Each time the foot of the tamper impacts the ground, a sensor attached to the footpad transmits the exact impact time. Impact signals and data are thus continuously transmitted to the recording instrument and then processed with cross-correlation. The source interval was 2 m, near offset 70 m, and a geophone spacing of 2 m was used. Recording was on a Geometrics Strata-View 48 channel exploration seismograph with a sample interval of 0.2 ms and a recording length of 400 ms. Because of the noisy environment, the quality of signal below 150 ms is poor, so the seismic profiles shown in this paper are cut off at 150 ms.

The seismic data were processed in a standard sequence as follows: pre-stack band-pass filter design and application; automatic gain control (AGC), muting of dead traces and refractions, and residual ground roll; geometry sort of data into CMP gather; velocity analysis; normal move-out corrections; CMP stack; post-stack band-pass filter; and appropriate display.

References

Allen, J.R.L., 1982. Sedimentary structures — their character and physical basis. Dev. Sedimentol. 30B (2), 1–663.

Allen, J.R.L., 1986. Earthquake magnitude-frequency, epicentral distance, and soft-sediment deformation in sedimentary basins. Sedimentology 46, 67–75.

Ambraseys, N.N., 1988. Engineering seismology; earthquake engineering and structural dynamics. J. Int. Assoc. Earthquake Engng 17, 1–105.

Angelier, J., Chu, H.-T., Lee, J.C., 1997. Shear concentration in a collision zone: kinematics of the Chihshang Fault as revealed by outcrop-scale quantification of active faulting, Longitudinal Valley, eastern. Tectonophysics 274, 117–143.

Angelier, J., Chu, H.-T., Lee, J.-C., Hu, J.-C., 2001. Active faulting and earthquake risk: the Chihshang Fault case, Taiwan. J. Geodyn. (in press).

Annan, A.P., Davis, J.L., 1976. Impulse radar sounding in permafrost. Radio Sci. 11, 383–394.

Audemard, A., de Santis, F., 1991. Survey of liquefaction structures induced by recent moderate earthquakes. Bull. Int. Assoc. Engng Geol. 44, 5–16.

Barrier, E., Chu, H.-T., 1984. Field trip guide to the Longitudinal Valley and the Coastal Range in eastern Taiwan. Field

Guidebook for the Sino-French Colloquium on Geodynamics of Eurasia–Philippine Sea Plate Boundary, Taipei, Taiwan, pp. 27–49.

Bilham, R., 1985. Subsurface Radar Imagery of Near-Surface Fractures Associated with the Borah Peak Earthquake. US Geological Survey Open-File Report 85-290-A. US Geological Survey, Denver, CO, pp. 182–194.

Bilham, R., Seeber, L., 1985. Paleoseismic Studies Using Subsurface Radar Profiling: Summaries of Technical Reports: 19. US Geological Survey Open-File Report 85-22. US Geological Survey, Denver, CO, 47 pp.

Chen, W.-S., 1988. Tectonic Evolution of Sedimentary Basins in the Coastal Range, Eastern Taiwan. PhD thesis, National Taiwan University, Taipei, Taiwan, 304 pp.

Chen, W.-S., 1991. Origin of the Lichi Mélange in the Coast Range, eastern Taiwan. Special Publication of the Central Geological Survey, vol. 5, pp. 257–266.

Chu, H.-T., Lee, J.-C., Angelier, J., 1994. Non-seismic rupture of the Tapo and the Chinyuan area on the southern segment of the Huatung Longitudinal Valley Fault, Eastern Taiwan. Soc. Geol. China, Annual Meeting, Taipei, pp. 1–5.

Chu, H.-T., Yü, M.-S., 1997. Study on the relationship between earthquake and faulting in the Taitung Longitudinal Valley, eastern Taiwan. NSC Report. Taipei, 133 pp (in Chinese).

Daniels, D.J., Gunton, D.J., Scott, H.F., 1988. Introduction to subsurface radar. IEE Proc. F 135 (4), 277–320.

Davis, J.L., Annan, A.P., 1989. Ground penetrating radar for high-resolution mapping of soil and rock stratigraphy. Geophys. Prospect. 37, 531–551.

Hsu, T.-L., 1962a. Recent faulting in the Longitudinal Valley of eastern Taiwan. Mem. Geol. Soc. China 1, 95–102.

Hsu, T.-L., 1962b. A study on the coastal geomorphology of Taiwan. Proc. Geol. Soc. China 5, 29–45.

Huang, C.-Y., Shyu, C.-T., Lin, S.-B., Lee, T.-Q., 1991. Marine geology in active arc-continent collision zone off southwestern Taiwan. Taicrust Workshop Proceedings, Taipei, Taiwan, pp. 227–235.

Lee, J.-C., Angelier, J., 1993. Localisation des déformations actives et traitement des données géodésiques: l'exemple de la faille de la Vallée Longitudinale, Taiwan. Bull. Soc. Géol. Fr. 164 (4), 533–570.

Lee, J.-C., 1994. Structure et déformation active d'un orogène, Taiwan. Mém. Sc. Terre Univ. P. et M. Curie, Paris, 94-17, 281 pp.

Moorman, B.J., 1990. Assessing the Ability of Ground Penetrating Radar to Delineate Subsurface Fluvial Lithofacies. Unpublished MSc thesis, Department of Geography, University of Calgary, Calgary, Alberta, Canada, 124 pp.

Sim, J.D., 1973. Earthquake-induced structures in sediments of Van Norman Lake, San Fernando, California. Science 182, 161–163.

Smith, D.G., Jol, H.M., 1995. Ground penetrating radar: antenna frequencies and maximum probable depths of penetration in Quaternary sediments. J. Appl. Geophys. 33, 93–100.

Tsai, Y.B., Teng, T.L., Chiu, J.M., Liu, H.L., 1977. Tectonic implications of the seismicity in the Taiwan region. Mem. Geol. Soc. China 2, 13–42.

Ulriksen, C.P.F., 1982. Application of Impulse Radar to Civil Engineering. Unpublished PhD thesis, Lund University of Technology, Lund, Sweden (republished by Geophysical Survey Systems Inc., Hudson, NH, 175 pp).

Yu, S.-B., Liu, C.-C., 1989. Fault creep on the central segment of the Longitudinal Valley Fault, eastern Taiwan. Proc. Geol. Soc. China 32 (3), 209–231.

Yu, S.-B., Jackson, D.-D., Yu, G.-K., Liu, C.-C., 1990. Dislocation model for crustal deformation in the Longitudinal Valley area, eastern Taiwan. Tectonophysics 183, 97–109.

Yu, S.-B., Chen, H.-Y., Kuo, L.-C., 1997. Velocity field of GPS stations in the Taiwan area. Tectonophysics 274 (1–3), 41–59.